Growth and optical properties of Nb-doped WS$_2$ monolayers

You may also be interested in:

Slidable atomic layers in van der Waals heterostructures
Yu Kobayashi, Takashi Taniguchi, Kenji Watanabe et al.

Photonics and optoelectronics of two-dimensional materials beyond graphene
Joice Sophia Ponraj, Zai-Quan Xu, Sathish Chander Dhanabalan et al.

Revealing the nature of excitons in liquid exfoliated monolayer tungsten disulphide
Kopotowski, C Backes, A A Mitioglu et al.

Photoluminescence of monolayer transition metal dichalcogenides integrated with VO2
Yu-Chuan Lin, Kursti DeLello, Hai-Tian Zhang et al.

Van der Waals stacked 2D layered materials for optoelectronics
Wenjing Zhang, Qixing Wang, Yu Chen et al.

Scalable synthesis of WS2 on graphene and h-BN: an all-2D platform for light-matter transduction
Antonio Rossi, Holger Büch, Carmine Di Rienzo et al.

Controllable growth of monolayer MoS2 by chemical vapor deposition via close MoO2 precursor for electrical and optical applications
Yong Xie, Zhan Wang, Yongjie Zhan et al.

Direct synthesis of large-area continuous ReS2 films on a flexible glass at low temperature
Youngchan Kim, Byunggil Kang, Yongsuk Choi et al.

Increased monolayer domain size and patterned growth of tungsten disulfide through controlling surface energy of substrates
Kyle Godin, Kyungnam Kang, Shichen Fu et al.

Growth and optical properties of Nb-doped WS$_2$ monolayers

Shogo Sasaki[1], Yu Kobayashi[1], Zheng Liu[2,3], Kazutomo Suenaga[3],
Yutaka Maniwa[1], Yuhei Miyauchi[4], and Yasumitsu Miyata[1,5*]

[1]*Department of Physics, Tokyo Metropolitan University, Hachioji, Tokyo 192-0397, Japan*
[2]*Inorganic Functional Materials Research Institute, AIST, Nagoya 463-8560, Japan*
[3]*Nanomaterials Research Institute, AIST, Tsukuba, Ibaraki 305-8565, Japan*
[4]*Institute of Advanced Energy, Kyoto University, Uji, Kyoto 611-0011, Japan*
[5]*JST, PRESTO, Kawaguchi, Saitama 332-0012, Japan*

*E-mail: ymiyata@tmu.ac.jp

We report the chemical vapor deposition growth of Nb-doped WS$_2$ monolayers and their characterization. Electron microscopy observations reveal that the Nb atom was substituted at the W site at a rate of approximately 0.5%. Unlike Mo doping, Nb-doped samples have photoluminescence (PL) peaks at 1.4–1.6 eV at room temperature. The peak energies are lower than the optical bandgap of 1.8 eV, and a saturation behavior of PL intensity is observed with the increase in excitation power. These results indicate that the observed PL peaks are assignable to the emission from impurity states generated by the substitution of Nb. © 2016 The Japan Society of Applied Physics

The optical properties of atomic-layer transition metal dichalcogenides (TMDCs) have recently attracted much attention owing to their wide-range bandgap energies from visible to infrared,[1–3] unique phenomena related to spin-valley physics,[4,5] and single-photon emission.[6–9] In particular, defect-derived excitonic states have recently received much attention for their applications in single-photon emitters. To date, several groups have reported that atomic-layer TMDCs show photoluminescence (PL) from optically active defects at low temperature (4 ∼ 90 K).[6–11] Such a two-dimensional (2D) single-quantum emission has practical advantages in efficient photon extraction and high integration capability. However, the details of such defect sites are still unclear, and PL can generally be observed only at low temperature. These issues may be resolved by the controlled fabrication of defect states, which is an important challenge in understanding and using TMDC atomic layers as quantum light sources.

In general, defect states in low-dimensional materials are created through several mechanisms, including atomic vacancy formation,[12] impurity doping,[13–16] and chemical functionalization.[17] In this study, we have investigated impurity-doped WS$_2$ monolayers as a model system. Monolayer WS$_2$ is a semiconductor with a relatively wide direct bandgap and high air stability, and there have been many reports on its growth process and characterization.[10,18–22] To implant impurities in WS$_2$, we employed halide-assisted chemical vapor deposition (CVD), which was recently developed by Li et al.[21] This method can produce large-area monolayer WS$_2$ at relatively low temperatures (700 °C) and under atmospheric pressure. Importantly, the use of halides can effectively transport precursors of transition metals, which usually have very low vapor pressure. As an impurity, Mo atoms are well studied and cause bandgap narrowing through the substitution of W sites in monolayer WS$_2$.[14,15,23,24] However, there are very few studies on the doping of other transition metals for monolayer TMDCs. In the present study, Nb is selected because its atomic size is comparable to that of Mo and it is reported to generate acceptor states for some TMDCs.[16,25]

Here, we report the synthesis and characterization of monolayer impurity-doped WS$_2$ using halide-assisted CVD.

Halide-assisted CVD was used to grow large-area monolayer Nb-doped WS$_2$ with a crystal size of 30 μm on a SiO$_2$ surface. Our scanning transmission electron microscopy (STEM) observations revealed that the Nb atom was substituted at the W site at a rate of approximately 0.5%. Unlike Mo doping, we found that Nb doping led to the appearance of new PL peaks between 1.4–1.6 eV at room temperature. The energies of these peaks were lower than the bandgaps (1.8 eV) estimated from differential reflectance spectra. Furthermore, the PL intensity exhibited a clear saturation behavior under the high-power excitation regime. These results indicate that the observed PL peaks are assignable to emission from the impurity state and that the present growth process could be used to fabricate TMDC atomic layers with controlled defect sites for single-photon applications.

Monolayer Nb-doped WS$_2$ crystals were grown on SiO$_2$/Si (285 nm SiO$_2$) and quartz substrates by using an in-house built CVD system [see Fig. 1(a)]. The substrate and a mixture of WO$_3$ (35 mg)/Nb (5 mg)/NaCl (15 mg) powders were placed at the center of a quartz tube. Sulfur flakes were placed 35 cm upstream of the center. The quartz tube was filled with Ar gas at a flow rate of 200 sccm under atmospheric pressure. The temperature of the substrate and powders was gradually increased to 830 °C over a period of 45 min by using an electrical furnace. When the substrate temperature reached the set point, the sulfur was heated at 200 °C for 15 min by using another electrical furnace to supply sulfur vapor to the substrate. After the reaction, the quartz tube was immediately cooled using an electric fan. As a reference sample, undoped WS$_2$ monolayers were grown under the same conditions without the use of Nb powder.

Optical images were recorded using an optical microscope (Nikon ECLIPSE-LV100D). Raman and PL measurements were conducted using a micro-Raman spectroscope (Renishaw inVia) with an excitation laser operating at 532 nm. A topography image of the samples was obtained by an atomic force microscope (AFM; Shimadzu SPM-9600) in tapping mode. Differential reflectance spectra were obtained by a spectrometer (Ocean Optics USB 2000+) with a white LED lamp. STEM observations were carried out by using a
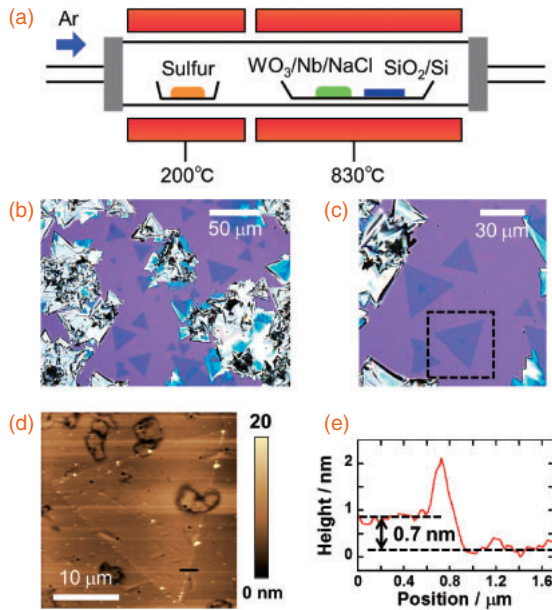
Fig. 1. (a) Illustration of CVD system used in the present study. (b, c) Optical microscope images of Nb-doped WS_2 monolayers and multilayers grown by halide-assisted CVD. (d) AFM image of the area indicated by a black box in (c). (e) Height profile of an Nb-doped WS_2 monolayer along the black line in (d).

JEM-2100F based electron microscope equipped with a JEOL Delta Cs corrector operated at 60 kV at 500 °C. For STEM observations, as-grown samples on SiO_2/Si substrates were covered with 1% poly(methyl methacrylate) (PMMA) in acetone by using a spin-coater. Then, the SiO_2 was etched by a 1 M KOH solution. After etching the substrate, the sample was washed twice by deionized water and picked up with an SiN membrane TEM grid. Finally, the PMMA was dissolved in acetone at 70 °C.

Figures 1(b) and 1(c) show optical microscopic images of typical crystals grown on SiO_2/Si substrates by halide-assisted CVD. Triangular crystals with a size of up to 30 μm and a relatively dark contrast are observed. The AFM image and height profile [Figs. 1(d) and 1(e)] reveal that the grain has a thickness of 0.7 nm, which corresponds to the thickness of a WS_2 monolayer.[20] It should be noted that the white triangular grains are multilayer grains. These results are similar WS_2 growth by halide-assisted CVD reported previously.[21]

For structural characterization, we conducted annular dark field (ADF)-STEM observations of a monolayer sample [Figs. 2(a) and 2(b) and Fig. S1 in the online supplementary

data at http://stacks.iop.org/APEX/9/071201/mmedia]. Because of their large atomic weight, W atoms exhibit a brighter ADF contrast than Nb and S atoms. In the present sample, the bright dots corresponding to W sites often become dark [Figs. 2(a) and 2(b)]. This can be assigned to the substitution of Nb atoms for W atoms [see Fig. 2(c)], as in the case of $Mo_{1-x}W_xS_2$ alloys and Re-doped MoS_2.[13,14,23] It should be noted that the STEM images of the doped samples are different from those of pure WS_2 monolayers as observed previously.[14] Through a statistical analysis of the ADF-STEM images obtained at six different positions of the same grain, the ratio of dark spots is estimated to be 0.55 ± 0.03%. It should be noted that it is quite difficult to conduct an elemental analysis on the present samples by electron energy loss spectroscopy (EELS) and energy-dispersive X-ray spectroscopy (EDX) because of the very weak signals from the Nb atoms. The Nb ratio of 0.55% is much smaller than the initial atomic ratio of Nb : W = 26 : 74 in the precursors. This indicates a very low supply rate of Nb, probably due to the fast oxidation of Nb. Indeed, Nb_2O_5 crystals were frequently observed on the substrates after growth in addition to the doped-WS_2 crystals. The suppression of Nb oxidation would be highly desirable and may be achieved using an alternative precursor for WO_3.

The substitutional doping is corroborated by Raman spectra of the doped WS_2 monolayers [Fig. 2(d)]. In these Raman spectra, two novel peaks are observed, at 379 and 401 cm^{-1}, in addition to major Raman modes, including the E′, A_1', and 2LA phonons of monolayer WS_2.[26] In a previous study of monolayer $Nb_{1-x}W_xS_2$, only a single peak at 383.4 cm^{-1} was observed under excitation with laser wavelength of 514 nm when x is decreased to 0.92, and the peak is assigned to 2H-type NbS_2-like A_1' mode from the peak position.[16] It should be noted that the present sample shows the two Raman peaks by doping in spite of much lower Nb concentration (approximately 0.5%) probably due to the resonance Raman effect.[26] In contrast, similar Raman peaks have been also found at 374 and 394 cm^{-1} in W-rich monolayer $Mo_{1-x}W_xS_2$ alloys ($x = 0.5$–0.9) grown by CVD.[15] In the $Mo_{1-x}W_xS_2$ alloy system, the low frequency peak at 374 cm^{-1} is interpreted as a MoS_2-like E′ mode from the polarization properties of Raman intensity.[27] Within this interpretation, the shift (5–7 cm^{-1}) in Raman frequencies is presumably caused by the difference in binding energy between the Nb–S and Mo–S bonds. It should be noted that the assignment of these Raman peaks requires further studies on polarization and resonance effects, and will be reported elsewhere.
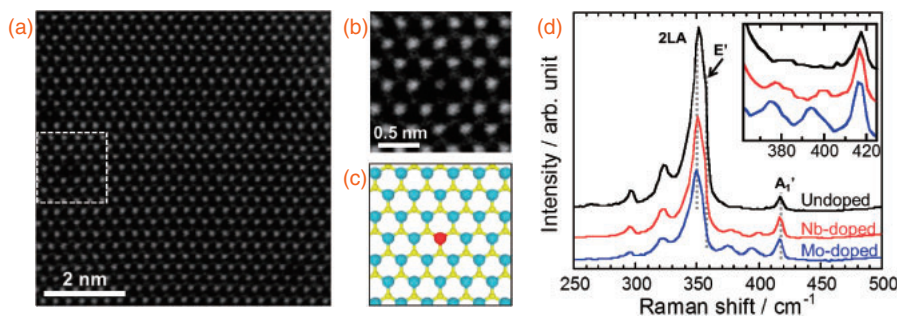

Fig. 2. (a) ADF-STEM image of Nb-doped monolayer WS_2. (b) Enlarged image and (c) structure model of the area indicated by a white box in a. Blue, red, and yellow spheres indicate W, Nb, S atoms, respectively. (d) Raman spectra of undoped, Nb-doped, and Mo-doped WS_2 monolayers. The spectra were normalized and shifted vertically for clarification.
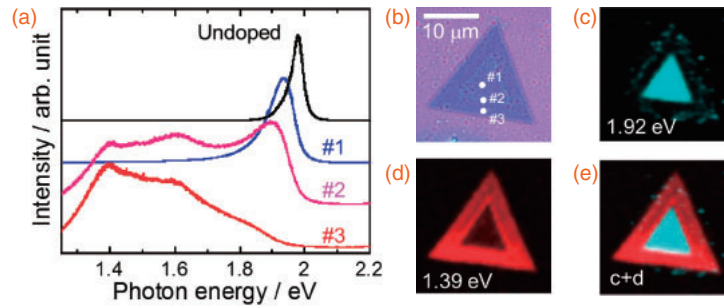
Fig. 3. (a) PL spectra of undoped and Nb-doped WS_2 monolayers at three different positions indicated in (b). The spectra were normalized and shifted vertically for clarity. (b) Optical micrograph and (c)–(e) PL intensity maps of a typical crystal of Nb-doped monolayer WS_2. Cyan and red indicate the PL intensities at 1.92 and 1.39 eV, respectively.
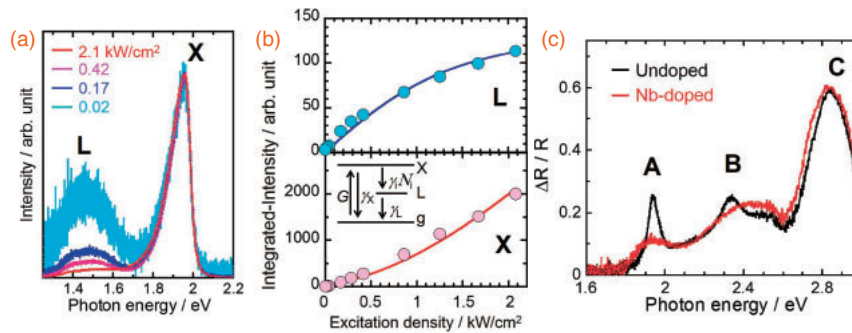

Fig. 4. (a) PL spectra of doped monolayer WS_2 grown on an SiO_2/Si substrate measured at four different laser powers. The spectra were normalized at 1.96 eV (b) PL intensities (solid circles) of L (upper panel) and X (lower panel) peaks plotted as a function of laser power. Lines indicate the fitting results. The inset shows a schematic of the three-level system of doped WS_2 consisting of the free (X) and localized (L) excitons, and ground (g) states. (c) Differential reflectance spectra for undoped and doped WS_2 monolayers grown on SiO_2 substrates.

Although the differences in the Raman spectra for Nb and Mo doping were small, we observed significant changes in the PL spectra for Nb-doped samples, which has never been observed for Mo doping in monolayer WS_2.[15,24,28] As seen in Fig. 3(a), undoped WS_2 monolayers have a PL peak at 1.98 eV, and the peak originates from the emission of free neutral and charged excitons. In contrast, the doped samples show new PL peaks at 1.4–1.6 eV, in addition to the peak at approximately 1.9 eV, and their PL spectra depend on the measurement position because of the gradient in doping concentration, as shown below. The peak at approximately 1.9 eV is assigned to emission from neutral and charged excitons, and is shifted toward lower energy by doping. The low-energy shift is observed for differential reflectance spectra [Fig. 4(c)], and is presumably derived from doping-induced bandgap narrowing.

It is noteworthy that individual grains have a composition gradient of Nb and W atoms. As seen in the PL intensity map [Figs. 3(c)–3(e)], the doping-induced emission at 1.39 eV is enhanced near the edge of grain, whereas the intensity at 1.92 eV becomes large in the interior of the grain. These results indicate that the Nb concentration increases towards the grain surface. Similar results have been obtained for CVD-grown monolayer $Mo_{1-x}W_xS_2$ alloys.[15,28] In the case of $Mo_{1-x}W_xS_2$, the supply rate of Mo atoms is higher than that of W atoms, which leads to the formation of heterostructures based on Mo-rich and W-rich $Mo_{1-x}W_xS_2$. In the present study, the PL data indicates that W atoms were supplied faster than Nb atoms through halide-assisted CVD.

The observed low-energy PL peaks at 1.4–1.6 eV can be assigned to emissions from localized excitons trapped in the potential induced by impurity atoms because of the following

reasons. Firstly, the intensity of a low-energy PL peak [L peak in Fig. 4(a)] is easily saturated under excitation with a laser power higher than $0.4 \, kW/cm^2$ [Figs. 4(a) and 4(b)]. In this power range, the high-energy PL peak [X peak in Fig. 4(a)] still increases. This saturation can be attributed to the low density of impurity sites coupled with the long lifetimes of localized states, as observed in previous reports. Indeed, the PL lifetime of similar defect states in WSe_2 monolayers has been reported to be approximately 1.79 ns, and a similar saturation behavior has been observed at 4.2 K.[9] This lifetime is much longer than the lifetime reported for A exciton of monolayers at low temperature (50–80 ps).[11,29] Note that the X peak shows superlinear behavior under excitation with laser powers higher than $0.4 \, kW/cm^2$. This can be explained by the effective blocking of the relaxation pass from free excitons to localized states owing to state filling. This leads to an increase in the lifetime and generation rate of free excitons, resulting in the superlinear behavior of peak X.

To qualitatively understand the nonlinear PL behavior, we used the rate equation model for a three-level system.[30,31] The three-level system consists of free excitons (X), localized excitons (L), and ground (g) states, as shown in the inset in Fig. 4(b). We considered the formation processes of localized excitons from free excitons trapped in impurity sites, and the filling of impurity states. The populations of free excitons $N_X(t)$ and localized excitons $N_L(t)$ at time t are expressed as

$$\frac{dN_X(t)}{dt} = G(t) - \gamma_X N_X(t) - \gamma_i [N_i - N_L(t)] N_X(t), \quad (1)$$

$$\frac{dN_L(t)}{dt} = \gamma_i [N_i - N_L(t)] N_X(t) - \gamma_L N_L(t), \quad (2)$$

S. Sasaki et al.

where $G(t)$ is the optical constant generation rate of free excitons, and N_i is the number density of impurity sites ($\sim 5.8 \times 10^{12} \, \text{cm}^{-2}$) estimated from the STEM results. The variables γ_X and γ_L are the decay rates of free and localized excitons, respectively, to the ground state, and γ_i is the formation rate coefficient of localized excitons from free excitons trapped in impurity sites. At room temperature, γ_X is tentatively estimated to be $(70 \, \text{ps})^{-1}$ from previous studies on undoped MoS_2 monolayers.[11,32] Under steady state conditions, the rate equations can be analytically solved as shown in the online supplementary data at http://stacks.iop.org/ APEX/9/071201/mmedia. The observed nonlinear behaviors are well reproduced by the calculated lines [Fig. 4(b)], when γ_L and $\gamma_i N_i$ are set to be $(10 \, \text{ns})^{-1}$ and $(22 \, \text{ps})^{-1}$, respectively. It should be noted that more precise measurements, including time-resolved PL, are desired for quantitative analysis of the decay rates.

Second, the emission of the L peak has lower energies than the absorption edge related to the interband optical transition. To gain insight into the electronic structure of doped samples, differential reflectance spectra were measured for undoped and doped WS_2 monolayers grown on quartz substrates [Figs. 4(c) and S2 in the online supplementary data at http:// stacks.iop.org/APEX/9/071201/mmedia]. It can be seen that the exciton absorption peaks A and B at, respectively, 1.94 and 2.34 eV become broadened. In contrast, almost no change is observed for peak C at 2.84 eV, which pertains to the optical transition of the band nesting region.[33] Importantly, the absorption edge is still located at approximately 1.8 eV even after doping. These results suggest that the electronic structure is not affected significantly by a Nb doping of approximately 0.5%. Nevertheless, excitons in WS_2 monolayers are very sensitive to doping because of the enhancement in inhomogeneous broadening and/or dephasing rate. A major factor of inhomogeneous broadening could be substitution-induced local changes of electronic structure as observed in the case of Mo doping.[23]

Finally, it should be noted that the doped samples have comparable integral intensities of PL peaks to the undoped WS_2. For example, the integral intensities at positions #1 and #3 in Fig. 3(a) are, respectively, almost the same as and half of that of the undoped sample. This suggests that the dopant atoms in WS_2 monolayers behave as optically active impurity sites. Because individual grains exhibit compositional gradients in Nb and W atoms, the present samples are useful for efficiently investigating the effects of impurity concentration on various chemical and physical properties, such as chemical reactivity, catalytic activity, charge transfer, quantum yield, valley polarization, and single photon emission. For single-photon emitter applications, it is highly desirable to decrease the impurity density and to find a good combination of impurity and TMDC atomic layers with high PL quantum yield. The present technique can be employed to prepare a wide variety of doped samples, and provide an efficient way to achieve carrier control in TMDC atomic layers. These samples are also essential for producing multifunctional lateral and vertical heterostructures based on TMDCs.

1) K. F. Mak, C. Lee, J. Hone, J. Shan, and T. F. Heinz, Phys. Rev. Lett. **105**, 136805 (2010).
2) A. Splendiani, L. Sun, Y. Zhang, T. Li, J. Kim, C.-Y. Chim, G. Galli, and F. Wang, Nano Lett. **10**, 1271 (2010).
3) W. Zhao, Z. Ghorannevis, L. Chu, M. Toh, C. Kloc, P.-H. Tan, and G. Eda, ACS Nano **7**, 791 (2013).
4) X. Xu, W. Yao, D. Xiao, and T. F. Heinz, Nat. Phys. **10**, 343 (2014).
5) K. F. Mak and J. Shan, Nat. Photonics **10**, 216 (2016).
6) M. Koperski, K. Nogajewski, A. Arora, V. Cherkez, P. Mallet, J. Y. Veuillen, J. Marcus, P. Kossacki, and M. Potemski, Nat. Nanotechnol. **10**, 503 (2015).
7) C. Chakraborty, L. Kinnischtzke, K. M. Goodfellow, R. Beams, and A. N. Vamivakas, Nat. Nanotechnol. **10**, 507 (2015).
8) A. Srivastava, M. Sidler, A. V. Allain, D. S. Lembke, A. Kis, and A. Imamoğlu, Nat. Nanotechnol. **10**, 491 (2015).
9) Y.-M. He, G. Clark, J. R. Schaibley, Y. He, M.-C. Chen, Y.-J. Wei, X. Ding, Q. Zhang, W. Yao, X. Xu, C.-Y. Lu, and J.-W. Pan, Nat. Nanotechnol. **10**, 497 (2015).
10) T. Kato and T. Kaneko, ACS Nano **8**, 12777 (2014).
11) T. Korn, S. Heydrich, M. Hirmer, J. Schmutzler, and C. Schüller, Appl. Phys. Lett. **99**, 102109 (2011).
12) W. Zhou, X. Zou, S. Najmaei, Z. Liu, Y. Shi, J. Kong, J. Lou, P. M. Ajayan, B. I. Yakobson, and J.-C. Idrobo, Nano Lett. **13**, 2615 (2013).
13) Y.-C. Lin, D. O. Dumcenco, H.-P. Komsa, Y. Niimi, A. V. Krasheninnikov, Y.-S. Huang, and K. Suenaga, Adv. Mater. **26**, 2857 (2014).
14) D. O. Dumcenco, H. Kobayashi, Z. Liu, Y.-S. Huang, and K. Suenaga, Nat. Commun. **4**, 1351 (2013).
15) Y. Kobayashi, S. Mori, Y. Maniwa, and Y. Miyata, Nano Res. **8**, 3261 (2015).
16) L.-P. Feng, W.-Z. Jiang, J. Su, L.-Q. Zhou, and Z.-T. Liu, Nanoscale **8**, 6507 (2016).
17) D. Voiry, A. Goswami, R. Kappera, S. C. de Carvalho Castro, D. Kaplan, T. Fujita, M. Chen, T. Asefa, and M. Chhowalla, Nat. Chem. **7**, 45 (2015).
18) Y. Kobayashi, S. Sasaki, S. Mori, H. Hibino, Z. Liu, K. Watanabe, T. Taniguchi, K. Suenaga, Y. Maniwa, and Y. Miyata, ACS Nano **9**, 4056 (2015).
19) M. Okada, T. Sawazaki, K. Watanabe, T. Taniguch, H. Hibino, H. Shinohara, and R. Kitaura, ACS Nano **8**, 8273 (2014).
20) H. R. Gutiérrez, N. Perea-López, A. L. Elías, A. Berkdemir, B. Wang, R. Lv, F. López-Urías, V. H. Crespi, H. Terrones, and M. Terrones, Nano Lett. **13**, 3447 (2013).
21) S. Li, S. Wang, D.-M. Tang, W. Zhao, H. Xu, L. Chu, Y. Bando, D. Golberg, and G. Eda, Appl. Mater. Today **1**, 60 (2015).
22) C. M. Orofeo, S. Suzuki, Y. Sekine, and H. Hibino, Appl. Phys. Lett. **105**, 083112 (2014).
23) S. Yoshida, Y. Kobayashi, R. Sakurada, S. Mori, Y. Miyata, H. Mogi, T. Koyama, O. Takeuchi, and H. Shigekawa, Sci. Rep. **5**, 14808 (2015).
24) Y. Chen, J. Xi, D. O. Dumcenco, Z. Liu, K. Suenaga, D. Wang, Z. Shuai, Y.-S. Huang, and L. Xie, ACS Nano **7**, 4610 (2013).
25) J. Suh, T.-E. Park, D.-Y. Lin, D. Fu, J. Park, H. J. Jung, Y. Chen, C. Ko, C. Jang, Y. Sun, R. Sinclair, J. Chang, S. Tongay, and J. Wu, Nano Lett. **14**, 6976 (2014).
26) A. Berkdemir, H. R. Gutiérrez, A. R. Botello-Méndez, N. Perea-López, A. L. Elías, C.-I. Chia, B. Wang, V. H. Crespi, F. López-Urías, J.-C. Charlier, H. Terrones, and M. Terrones, Sci. Rep. **3**, 1755 (2013).
27) Y. Chen, D. O. Dumcenco, Y. Zhu, X. Zhang, N. Mao, Q. Feng, M. Zhang, J. Zhang, P.-H. Tan, Y.-S. Huang, and L. Xie, Nanoscale **6**, 2833 (2014).
28) S. Zheng, L. Sun, T. Yin, A. M. Dubrovkin, F. Liu, Z. Liu, Z. X. Shen, and H. J. Fan, Appl. Phys. Lett. **106**, 063113 (2015).
29) Y. You, X.-X. Zhang, T. C. Berkelbach, M. S. Hybertsen, D. R. Reichman, and T. F. Heinz, Nat. Phys. **11**, 477 (2015).
30) N. Akizuki, M. Iwamura, S. Mouri, Y. Miyauchi, T. Kawasaki, H. Watanabe, T. Suemoto, K. Watanabe, K. Asano, and K. Matsuda, Phys. Rev. B **89**, 195432 (2014).
31) S. Mouri, Y. Miyauchi, and K. Matsuda, Nano Lett. **13**, 5944 (2013).
32) H. Shi, R. Yan, S. Bertolazzi, J. Brivio, B. Gao, A. Kis, D. Jena, H. G. Xing, and L. Huang, ACS Nano **7**, 1072 (2013).
33) D. Kozawa, R. Kumar, A. Carvalho, K. Kumar Amara, W. Zhao, S. Wang, M. Toh, R. M. Ribeiro, A. H. Castro Neto, K. Matsuda, and G. Eda, Nat. Commun. **5**, 4543 (2014).